Development of continuum-based particle models of cell growth and proliferation for simulating tissue morphogenesis

AUTHOR(S):

Yokoyama, Yuka; Kameo, Yoshitaka; Adachi, Taiji

CITATION:

Yokoyama, Yuka ...[et al]. Development of continuum-based particle models of cell growth and proliferation for simulating tissue morphogenesis. Journal of the Mechanical Behavior of Biomedical Materials 2023, 142: 105828.

ISSUE DATE:

2023-04

URL:

http://hdl.handle.net/2433/282142

journal of the mechanical behavior of biomedical materials 142 (2023) 105828

Contents lists available at ScienceDirect

Journal of the Mechanical Behavior of Biomedical Materials

journal homepage: www.elsevier.com/locate/jmbbm

Development of continuum-based particle models of cell growth and proliferation for simulating tissue morphogenesis

Yuka Yokoyama [a], Yoshitaka Kameo [a,b,c], Taiji Adachi [a,b,c,*]

[a] Department of Micro Engineering, Graduate School of Engineering, Kyoto University, 53 Shogoin-Kawahara-cho, Sakyo, Kyoto, 606-8507, Japan
[b] Department of Biosystems Science, Institute for Life and Medical Sciences, Kyoto University, 53 Shogoin-Kawahara-cho, Sakyo, Kyoto, 606-8507, Japan
[c] Department of Mammalian Regulatory Network, Graduate School of Biostudies, Kyoto University, 53 Shogoin-Kawahara-cho, Sakyo, Kyoto, 606-8507, Japan

ARTICLE INFO

Keywords:
Morphogenesis
Growth
Proliferation
Continuum-based particle modeling
Material point method
Computational biomechanics

ABSTRACT

Biological tissues acquire various characteristic shapes through morphogenesis. Tissue shapes result from the spatiotemporally heterogeneous cellular activities influenced by mechanical and biochemical environments. To investigate multicellular tissue morphogenesis, this study aimed to develop a novel multiscale method that can connect each cellular activity to the mechanical behaviors of the whole tissue by constructing continuum-based particle models of cellular activities. This study proposed mechanical models of cell growth and proliferation that are expressed as volume expansion and cell division by extending the material point method. By simulating cell hypertrophy and proliferation under both free and constraint conditions, the proposed models demonstrated potential for evaluating the mechanical state and tracing cells throughout tissue morphogenesis. Moreover, the effect of a cell size checkpoint was incorporated into the cell proliferation model to investigate the mechanical behaviors of the whole tissue depending on the condition of cellular activities. Consequently, the accumulation of strain energy density was suppressed because of the influence of the checkpoint. In addition, the whole tissues acquired different shapes depending on the influence of the checkpoint. Thus, the models constructed herein enabled us to investigate the change in the mechanical behaviors of the whole tissue according to each cellular activity depending on the mechanical state of the cells during morphogenesis.

1. Introduction

Morphogenesis is a dynamic process of tissue formation in response to mechanical forces generated by cellular activities, such as proliferation, hypertrophy, apoptosis, and contraction (Green et al., 2015; Heer and Martin, 2017; Matejčić and Trepat, 2022; Trubuil et al., 2021). Through morphogenesis, biological tissues acquire various characteristic shapes depending on spatiotemporally heterogeneous cellular activities, which are affected by mechanical and biochemical environments (Chanet et al., 2017; Felsenthal and Zelzer, 2017; Green et al., 2015; Heer and Martin, 2017; Shwartz et al., 2012). Because of the complicated regulation mechanism of the mechanical behaviors of the whole tissue via microscopic cellular activities, a comprehensive understanding of this multiscale mechanism of morphogenesis through *in vivo* and *in vitro* experiments has been challenging.

To examine the mechanism of morphogenesis, modeling and simulation approaches aid in determining effective strategies (Montes-Olivas et al., 2019; Osborne et al., 2017). One of the major strategies is discrete modeling of each cellular activity using vertex models, subcellular models, and cellular Potts models (Alt et al., 2017; Jamali et al., 2010; Voss-Böhme, 2012). Although these models effectively express microscopic cellular activities, quantitative evaluation of the mechanical behaviors of the whole tissue is challenging because the constitutive relationship at the tissue level cannot be specified in discrete models. Another strategy is the modeling of tissue morphogenesis based on continuum mechanics (Conte et al., 2008; Takeda et al., 2019; Vaca-González et al., 2018). Using the finite element method (FEM), which incorporates the constitutive law of tissues, these models can effectively evaluate the mechanical behaviors of the whole tissue as a continuum body. However, evaluating the spatiotemporally heterogeneous cellular activities at a single-cell level is difficult in FEM. Therefore, a novel approach using a multiscale model that can connect each cellular activity to the mechanical behaviors of the whole tissue is indispensable.

The material point method (MPM) is a promising strategy for the

Abbreviations: EBS, Extended B-splines; FEM, Finite element method; MPM, Material point method.

* Corresponding author. 53 Shogoin-Kawahara-cho, Sakyo, Kyoto, 606-8507, Japan.
E-mail address: adachi@infront.kyoto-u.ac.jp (T. Adachi).

https://doi.org/10.1016/j.jmbbm.2023.105828
Received 5 December 2022; Received in revised form 28 March 2023; Accepted 2 April 2023
Available online 11 April 2023

multiscale simulation of tissue morphogenesis. It is mainly used in geotechnical engineering and graphics (Bardenhagen and Kober, 2004; Charlton et al., 2017; Pan et al., 2021; Stomakhin et al., 2013; Yamaguchi et al., 2021). The MPM is a hybrid method that combines the advantages of both Lagrangian and Eulerian methods, in which physical domains are represented by discrete Lagrangian material points, whereas the equilibrium equation based on continuum mechanics is solved using Eulerian background grid nodes. By assuming a discrete material point as a biological cell and incorporating cellular activities as behaviors of a material point, each cellular activity will be connected to the mechanical behaviors of the whole tissue.

To develop a multiscale method of investigating multicellular tissue morphogenesis that can connect each cellular activity to the mechanical behaviors of the whole tissue, we aimed to extend the MPM by constructing continuum-based particle models of cellular activities. We constructed cell growth and proliferation models to represent cellular activities contributing to tissue morphogenesis. To show the validity of the proposed models, we simulated cell hypertrophy and proliferation under both free and constraint conditions. Moreover, to demonstrate the potential of the method to simulate tissue morphogenesis depending on the condition of cellular activities, we incorporated the effect of a cell size checkpoint (Liu et al., 2018; Xie and Skotheim, 2020) into the cell proliferation model and examined the effect of the checkpoint on the mechanical behaviors of the whole tissue.

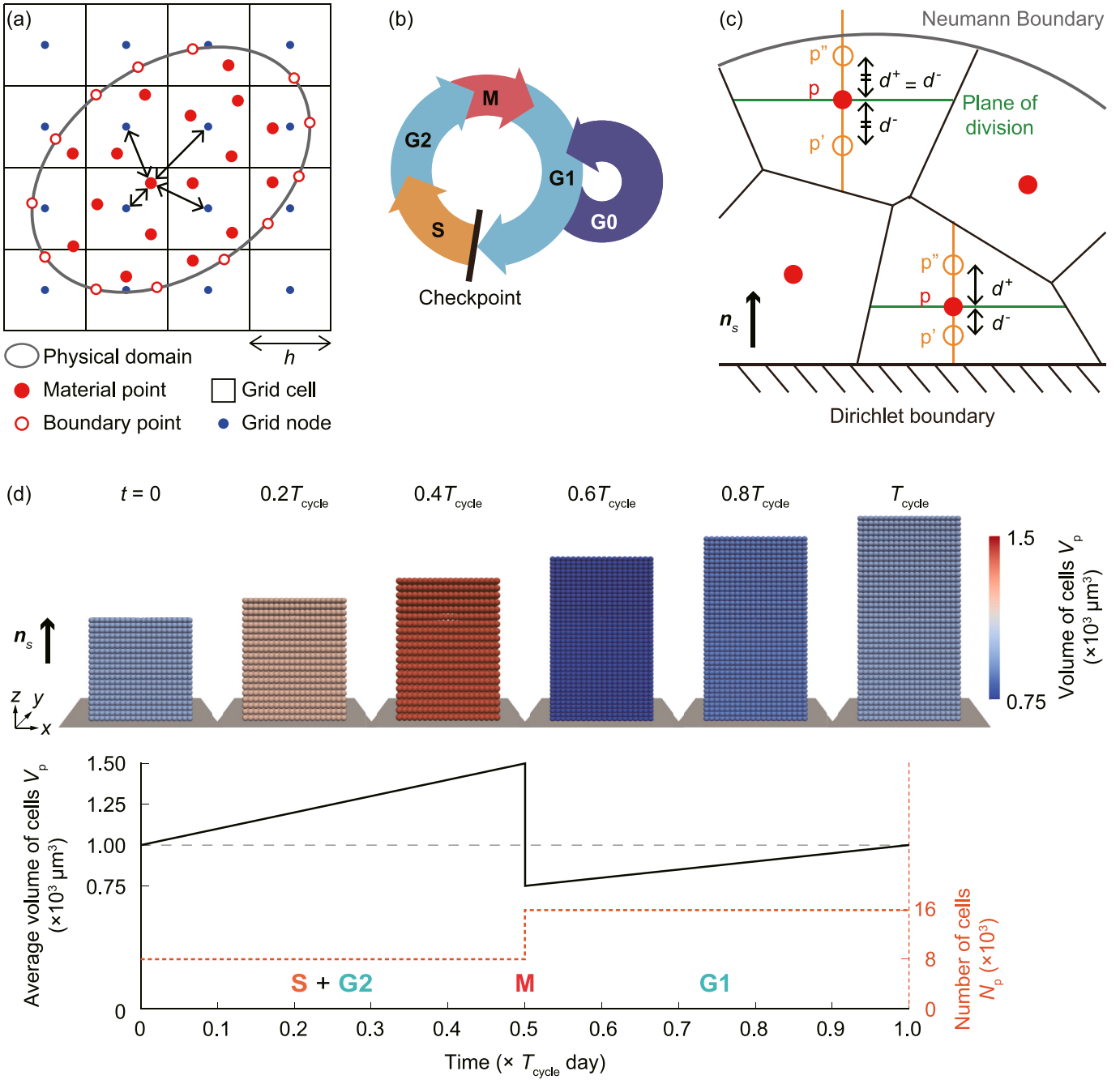

Fig. 1. Concept of the material point method (MPM) and the cell proliferation model. (a) The physical domain and its boundary in the MPM. (b) A cell cycle composed of S (DNA replication), G2, M (mitosis), G1, and G0 (quiescence) phases. (c) Placement of points after the division in the cell proliferation model. (d) Implementation of the cell proliferation model. Change in the average cell volume V_p and number of cells N_p according to the cell proliferation are graphed.

2. Materials and methods

2.1. Material point method

Let Ω^0 and Ω be the physical domains in the initial and current configurations, respectively, of a biological tissue composed of numerous cells, which was modeled as a continuum body. The boundary of the current configuration $\partial\Omega$ is exclusively divided into the Neumann boundary $\partial\Omega_\sigma$ and Dirichlet boundary $\partial\Omega_u$, as $\partial\Omega = \partial\Omega_\sigma \cup \partial\Omega_u$. The prescribed surface traction force vector $\bar{\boldsymbol{t}}$ is imposed as $\boldsymbol{t} = \boldsymbol{\sigma n} = \bar{\boldsymbol{t}}$ on $\partial\Omega_\sigma$, and displacement vector $\bar{\boldsymbol{u}}$ is imposed as $\boldsymbol{u} = \bar{\boldsymbol{u}}$ on $\partial\Omega_u$, where variables $\boldsymbol{t}$, $\boldsymbol{u}$, $\boldsymbol{\sigma}$, and $\boldsymbol{n}$ are the surface force vector, displacement vector, Cauchy stress tensor, and outward unit normal vector on the boundary, respectively. The body force vector $\boldsymbol{b}$ is assumed to act over the current physical domain Ω. Tissue deformation caused by cell growth and proliferation was assumed as a quasi-static process. Therefore, the principle of virtual work can be expressed as

$$\int_\Omega \boldsymbol{\sigma} : \delta\boldsymbol{\varepsilon} dv = \int_{\partial\Omega_\sigma} \bar{\boldsymbol{t}} \cdot \delta\boldsymbol{u} ds + \int_\Omega \boldsymbol{b} \cdot \delta\boldsymbol{u} dv, \tag{1}$$

where $\delta\boldsymbol{u}$ and $\delta\boldsymbol{\varepsilon}$ are the virtual displacement vector and first variation of the Euler–Almansi strain tensor and dv and ds are infinitesimal volume and surface elements in the current configuration, respectively.

To investigate the mechanical behaviors of the whole tissue caused by each cellular activity in morphogenesis based on continuum mechanics, we employed the MPM (Bardenhagen and Kober, 2004). In the MPM, the physical domain and its boundary are represented by material and boundary points, respectively (Fig. 1 (a)). A material point p possesses the position vector $\boldsymbol{x}_\mathrm{p}$, deformation gradient tensor $\boldsymbol{F}_\mathrm{p}$, and volume V_p. A boundary point pb possesses the position vector $\boldsymbol{x}_\mathrm{pb}$, deformation gradient tensor $\boldsymbol{F}_\mathrm{pb}$, and area a_pb. By using these points, each term in Eq. (1) is discretized as follows:

$$\int_\Omega \boldsymbol{\sigma} : \delta\boldsymbol{\varepsilon} dv \approx \sum_{\mathrm{p\ in\ }\Omega} \boldsymbol{\sigma}_\mathrm{p} : \delta\boldsymbol{\varepsilon}\left(\boldsymbol{x}_\mathrm{p}\right) V_\mathrm{p}, \tag{2}$$

$$\int_{\partial\Omega_\sigma} \bar{\boldsymbol{t}} \cdot \delta\boldsymbol{u} ds \approx \sum_{\mathrm{pb\ on\ }\partial\Omega_\sigma} \bar{\boldsymbol{t}}_\mathrm{pb} \cdot \delta\boldsymbol{u}\left(\boldsymbol{x}_\mathrm{pb}\right) a_\mathrm{pb}, \tag{3}$$

$$\int_\Omega \boldsymbol{b} \cdot \delta\boldsymbol{u} dv \approx \sum_{\mathrm{p\ in\ }\Omega} \boldsymbol{b}_\mathrm{p} \cdot \delta\boldsymbol{u}\left(\boldsymbol{x}_\mathrm{p}\right) V_\mathrm{p}, \tag{4}$$

where subscripts p and pb are assigned to variables of the material point p and boundary point pb, respectively. In this study, we considered a material point as a single-cell so that we can explicitly represent cell growth and division.

The displacement field $\boldsymbol{u}(\boldsymbol{x})$ at position $\boldsymbol{x}$ is discretized by Eulerian grid nodes as

$$\boldsymbol{u}(\boldsymbol{x}) \approx \sum_\mathrm{g} \boldsymbol{u}_\mathrm{g} N_\mathrm{g}(\boldsymbol{x}), \tag{5}$$

where $\boldsymbol{u}_\mathrm{g}$ is the displacement vector at grid node g and $N_\mathrm{g}(\boldsymbol{x})$ is an interpolation function for the grid node g. To suppress numerical instability, quadratic extended B-splines (EBS) (Yamaguchi et al., 2021) defined on a regular background grid with grid spacing h were chosen for the interpolation function $N_\mathrm{g}(\boldsymbol{x})$. The occupation parameter, C_C, which is used to activate/inactivate the EBS on the grid nodes near the boundary of the physical domain, was chosen as $C_C = 0.85$. To impose the Dirichlet boundary condition for $\boldsymbol{u}$ ($\boldsymbol{u} = \bar{\boldsymbol{u}}$ on $\partial\Omega_u$), Nitsche's method was employed (Yamaguchi et al., 2021). The penalty parameter for Nitsche's method, β, which is used for the penalty term similar to that in the standard penalty method, was set as $\beta = 1.0 \times 10^3 \frac{E}{h}$, where E is Young's modulus.

The mechanical behaviors of the whole tissue, depending on each cellular activity, were calculated for the discrete time increments Δt. The principle of virtual work, Eq (1), was solved using the state variables of material and boundary points at time t with respect to the displacement at grid nodes $\boldsymbol{u}_\mathrm{g}$ using the Newton–Raphson procedure. After the calculation, the position $\boldsymbol{x}_\mathrm{p}$, deformation gradient $\boldsymbol{F}_\mathrm{p}$, and volume V_p of the material point p at time $t + \Delta t$ were calculated according to

$$\boldsymbol{x}_\mathrm{p}^{t+\Delta t} = \boldsymbol{x}_\mathrm{p}^t + \sum_\mathrm{g} \boldsymbol{u}_\mathrm{g} N_\mathrm{g}\left(\boldsymbol{x}_\mathrm{p}^t\right), \tag{6}$$

$$\boldsymbol{F}_\mathrm{p}^{t+\Delta t} = \left(\mathbf{I} + \sum_\mathrm{g} \boldsymbol{u}_\mathrm{g} \otimes \frac{\partial N_\mathrm{g}\left(\boldsymbol{x}_\mathrm{p}^t\right)}{\partial \boldsymbol{x}}\right) \boldsymbol{F}_\mathrm{p}^t, \tag{7}$$

$$V_\mathrm{p}^{t+\Delta t} = \det \boldsymbol{F}_\mathrm{p}^{t+\Delta t} V_\mathrm{p}^0 \tag{8}$$

The position $\boldsymbol{x}_\mathrm{pb}$, deformation gradient $\boldsymbol{F}_\mathrm{pb}$, and area a_pb of the boundary point pb at time $t + \Delta t$ were calculated according to

$$\boldsymbol{x}_\mathrm{pb}^{t+\Delta t} = \boldsymbol{x}_\mathrm{pb}^t + \sum_\mathrm{g} \boldsymbol{u}_\mathrm{g} N_\mathrm{g}\left(\boldsymbol{x}_\mathrm{pb}^t\right), \tag{9}$$

$$\boldsymbol{F}_\mathrm{pb}^{t+\Delta t} = \left(\mathbf{I} + \sum_\mathrm{g} \boldsymbol{u}_\mathrm{g} \otimes \frac{\partial N_\mathrm{g}\left(\boldsymbol{x}_\mathrm{pb}^t\right)}{\partial \boldsymbol{x}}\right) \boldsymbol{F}_\mathrm{pb}^t, \tag{10}$$

$$a_\mathrm{pb}^{t+\Delta t} \boldsymbol{n}_\mathrm{pb}^{t+\Delta t} = \det \boldsymbol{F}_\mathrm{pb}^{t+\Delta t} \left(\boldsymbol{F}_\mathrm{pb}^{t+\Delta t}\right)^{-\mathrm{T}} a_\mathrm{pb}^0 \boldsymbol{n}_\mathrm{pb}^0 \tag{11}$$

Here, superscripts $t, t + \Delta t$ are assigned to the variables at time $t, t + \Delta t$, respectively. The values V_p^0, a_pb^0, and $\boldsymbol{n}_\mathrm{pb}^0$ indicate the volume, area, and outward unit normal vector in the initial configuration Ω^0, respectively.

2.2. Cell growth model

To express cell growth in tissue morphogenesis, we constructed a cell growth model for the MPM based on the theory of finite growth (Himpel, G., Kuhl, E., Menzel, A., & Steinmann, 2005; Takeda et al., 2019). In this study, we assumed a multiplicative decomposition of the deformation gradient at material point p as

$$\boldsymbol{F}_\mathrm{p} = \boldsymbol{F}_\mathrm{p}^\mathrm{e} \boldsymbol{F}_\mathrm{p}^\mathrm{g}, \tag{12}$$

where $\boldsymbol{F}_\mathrm{p}^\mathrm{e}$ and $\boldsymbol{F}_\mathrm{p}^\mathrm{g}$ are an elastic part and a growth part of the deformation gradient, respectively. The isotropic growth of a composing cell was imposed by setting the growth part of the deformation gradient at the corresponding material point $\boldsymbol{F}_\mathrm{p}^\mathrm{g}$ as

$$\boldsymbol{F}_\mathrm{p}^\mathrm{g} = \theta \mathbf{I}, \tag{13}$$

where θ and $\mathbf{I}$ are growth stretch and the second-order identity tensor, respectively.

The biological tissue was modeled as a hyperelastic material following the compressible neo-Hookean model (Chagnon et al., 2015; Himpel, G., Kuhl, E., Menzel, A., & Steinmann, 2005), in which strain energy density Ψ is expressed as,

$$\Psi = \frac{\lambda}{8} \ln^2 I_3 + \frac{\mu}{2} (I_1 - 3 - \ln I_3) \tag{14}$$

In this equation, μ and λ are Lame's constants, I_1 and I_3 are the first and third invariants of the elastic part of the right Cauchy–Green tensor, $\boldsymbol{C}_\mathrm{p}^\mathrm{e} = \boldsymbol{F}_\mathrm{p}^{\mathrm{e}\mathrm{T}} \boldsymbol{F}_\mathrm{p}^\mathrm{e}$, respectively. According to this theory, an increase in the volume at the material point is represented by increasing the growth stretch θ.

2.3. Cell proliferation model

To express cell proliferation in tissue morphogenesis, we constructed a cell proliferation model for the MPM by combining the unidirectional growth and division of material points. The state of each proliferative cell was classified into S (DNA replication), G2, M (mitosis), G1, and G0 (quiescence) phases (Fig. 1 (b)). Let $\pm\boldsymbol{n}_s$ be unit normal vectors of the plane of division for a material point p (Fig. 1 (c)). For T_{cycle}, total duration of S, G2, M, and G1 phases, a cell was assumed to grow unidirectionally and constantly by updating the growth part of the deformation gradient at the corresponding material point $\boldsymbol{F}_p^g$ as

$$\boldsymbol{F}_p^g = (\mathbf{I} + (\theta - 1)\boldsymbol{n}_s \otimes \boldsymbol{n}_s)\boldsymbol{F}_{p\_pre}^g, \tag{15}$$

where $\boldsymbol{F}_{p\_pre}^g$ is the growth part of the deformation gradient before the onset of the S phase. The growth stretch θ increased from 1.0 to 2.0 at a constant rate within T_{cycle}.

In the M phase, mitosis was modeled as a division of the material point p into two material points p′ and p″ at the time point of $\frac{T_{cycle}}{2}$ after the onset of the S phase (Fig. 1 (d)). Here, the position, deformation gradient, and volume of the new material points were provided as

$$\boldsymbol{x}_{p'} = \boldsymbol{x}_p - d^-\boldsymbol{n}_s, \boldsymbol{x}_{p''} = \boldsymbol{x}_p + d^+\boldsymbol{n}_s, \tag{16}$$

$$\boldsymbol{F}_{p'} = \boldsymbol{F}_p, \boldsymbol{F}_{p''} = \boldsymbol{F}_p, \tag{17}$$

$$V_{p'} = \frac{1}{2}V_p, V_{p''} = \frac{1}{2}V_p, \tag{18}$$

where d^- and d^+ are the distance between the new material points and the original material point (Fig. 1 (c)). To determine d^- and d^+, we considered a three-dimensional Voronoi diagram constructed using all material points as generating points, which expresses cell shapes. In this diagram, new material points p′ and p″ were positioned at the middle point of the original material point p and Voronoi or Dirichlet boundary in the negative and positive $\boldsymbol{n}_s$ directions from the original material point, respectively (Fig. 1 (c)). If a material point had no adjacent Voronoi nor Dirichlet boundary in either $-\boldsymbol{n}_s$ or $+\boldsymbol{n}_s$ directions, a new material point for the corresponding direction was placed to satisfy

$$d^+ = d^-, \tag{19}$$

using the distance in the other direction. If a material point has neither adjacent Voronoi nor Dirichlet boundary in both $-\boldsymbol{n}_s$ and $+\boldsymbol{n}_s$ directions, new material points were placed by setting

$$d^+ = \frac{1}{4}\sqrt[3]{V_p}, d^- = \frac{1}{4}\sqrt[3]{V_p}, \tag{20}$$

where we assumed the representative length of material points to be $\sqrt[3]{V_p}$.

After a cell cycle, the cell goes into the quiescent G0 phase to wait for the onset of the next cell cycle. The length of the G0 phase was assumed to follow an exponential distribution with the rate parameter λ.

Fig. 1 (d) presents an example of cell proliferation in a cubic tissue placed on a plane with a slip boundary condition. All composing cells proliferated simultaneously with the same plane of division by setting $\boldsymbol{n}_s$ as a unit vector along the z-axis. In this case, the number of cells N_p was exactly doubled, and the volume of each cell V_p after the cell cycle ($t = T_{cycle}$) was the same as the initial volume ($t = 0$).

2.4. Parameter setting

In this study, Young's modulus and Poisson's ratio were chosen as $E = 1.0$ kPa and $\nu = 0.4$, respectively, by considering the order of the values of chondrocytes (Luo et al., 2016; Trickey et al., 2006). The length of a cell cycle T_{cycle} was set to 1 day.

2.5. Grid spacing dependency

In the MPM, the principle of virtual work, Eq (1), is solved for the displacement specified on background grid nodes. Therefore, the accuracy of the simulation mainly depends on the grid spacing h, and the smaller value of h enables a more accurate analysis. Under the condition with the same value of h, the larger value of the number of material points per grid spacing, $N_{p/h}$, makes the analysis more accurate (Yamaguchi et al., 2021). A too small value of $N_{p/h}$ even leads failure simulation. Thus, $N_{p/h} = 5$–10 was used in a previous study (Yamaguchi et al., 2021). In the present study, we set the representative length of material points, which corresponds to the material point spacing in the initial condition, to $L_p = 10$ μm, as the size of the same order as biological cells.

Accordingly, we examined the dependency of the simulation on the grid spacing h by conducting simulations of large deformation of growing multicellular tissues. In this study, the initial shape of the whole tissue was set as a sphere with a diameter of 500 μm , composed of regularly distributed 6.6×10^4 material points and covered by 2.6×10^3 boundary points. The tissue grew isotropically according to the increase in the growth stretch θ depicted in Eq. (13), with the surface of the lower half fixed. We set the grid spacing h as 33 μm ($N_{p/h} = 3.3$), 50 μm ($N_{p/h} = 5.0$), 75 μm ($N_{p/h} = 7.5$), and 100 μm ($N_{p/h} = 10$) and compared the shape of the whole tissues when $\theta = 1.4$ (Fig. 2 (a–d)). As a high-resolution reference, another simulation, in which the representative length of material points L_p was set to 5.0 μm and the grid spacing h was set to 25 μm ($N_{p/h} = 5.0$), is also illustrated in Fig. 2 (e). In this case, the tissue was composed of 5.2×10^5 material points and covered by 2.6×10^3 boundary points. As a result of the high-resolution simulation, the unconstrained upper half of the tissue demonstrated a hemispheric shape with a constant curvature (Fig. 2 (e)). By comparing the results for $L_p = 10$ μm (Fig. 2 (a–d)) with the result for $L_p = 5.0$ μm (Fig. 2 (e)), the results with $h = 33$ and 50 μm are considered sufficiently accurate (Fig. 2 (f, g)). As the grid spacing h increased to 75 or 100 μm, the tissue shape became distorted, indicating less accuracy (Fig. 2 (c, d)), although $N_{p/h}$ was in the range of 5–10. Therefore, we chose $h = 50$ μm ($N_{p/h} = 5.0$) for all the following simulations.

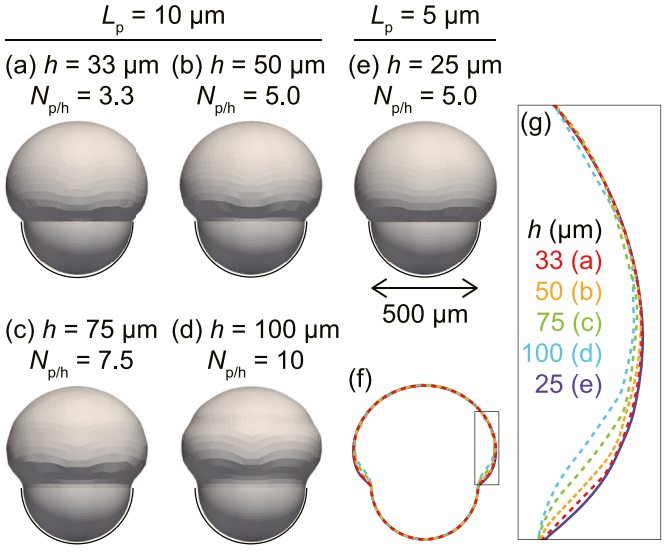

Fig. 2. Dependency of tissue shapes on the grid spacing h. (a–e) Outer shapes of growing tissues at $\theta = 1.4$ with grid spacings of (a) 33, (b) 50, (c) 75, (d) 100, and (e) 25 μm. The representative length of material points L_p is 10 μm for (a–d) and 5 μm for (e). (f) Outline of the tissues. (g) Magnified image of the boxed area on (f).

3. Results

3.1. Verification of cell growth and proliferation models

To verify the constructed models of cell growth and proliferation, we simulated cell hypertrophy and proliferation in a cubic tissue placed on a plane with a slip boundary condition (Fig. 3). In the initial state, the edge size of the cubic tissue was set to 200 μm. The tissue was composed of regularly distributed 8.0×10^3 material points and covered by 2.9×10^3 boundary points. Fig. 3 (a) depicts the results of cell hypertrophy simulation based on the cell growth model, in which cells in the tissue grew isotropically with the same rate of increase in growth stretch θ presented in Eq. (13). The isotropic growth of the whole tissue and uniform volume expansion of composing cells V_p were successfully simulated. In this study, the value of internal residual stress was negligible, indicating that the free boundary condition was properly imposed in the simulation. Fig. 3 (b) presents the result of the cell proliferation simulation, in which cells in the tissue proliferate with random planes of division at random timings with the rate parameter $\lambda = 1.0$/day/cell. As illustrated in Fig. 3 (b), the generation (top) and cell volume V_p (middle) became heterogeneous, and the strain energy density Ψ_p (bottom) sporadically concentrated at a single-cell level because of random proliferation. In the random proliferation, the number of cells N_p and the total volume of the tissue V_tot increased exponentially (Fig. 3 (c, d)) and the average strain energy density Ψ_ave increased linearly (Fig. 3 (e)). These mechanical behaviors of the whole tissue were independent of the random selection of division planes and timings (data not shown). Accordingly, cell hypertrophy and proliferation were successfully expressed, and the mechanical behaviors of the whole tissue were examined by the simulation based on our constructed models.

3.2. Simulation of tissue morphogenesis

Considering the condition of tissues growing *in vivo* where the tissue of interest is partially constrained by surrounding tissues, such as immature bone tissue covered by calcified bone collar (Kronenberg, 2003), we simulated proliferation under a constraint condition, as is the case illustrated in Fig. 2. Again, the initial shape of the whole tissue was set as a sphere with a diameter of 500 μm, composed of regularly distributed 6.6×10^4 material points and covered by 2.6×10^3 boundary points. The cells that composed the tissue proliferate with random planes of division at random timings with the rate parameter $\lambda = 1.0$/day/cell. Fig. 4 (a) presents the simulation result with the surface of the lower half fixed. Because of the constraint condition, cells with relatively large volume V_p were observed only in the upper half of the tissue (red cells in Fig. 4 (a)).

To depict the potential of the proposed method of investigating the mechanical behaviors of the whole tissue depending on the condition of cellular activities, the effect of a cell size checkpoint (Liu et al., 2018; Xie and Skotheim, 2020) was incorporated into the cell proliferation model. Cell size is known to be maintained by regulating the timing of cell division (Lloyd, 2013). Although the mechanism underlying this regulation remains controversial, several lines of evidence suggested a possible mechanism that cells should reach a critical size before passing the decision point for entry into the S phase from the G1 or G0 phase, which is called a cell size checkpoint (Fig. 1 (b)) (Liu et al., 2018; Xie and Skotheim, 2020). To evaluate the effect of this checkpoint on tissue morphogenesis, we assumed that if the volume ratio of the material point p to the initial cell volume, $J_\mathrm{p}^\mathrm{e} = \det \boldsymbol{F}_\mathrm{p}^\mathrm{e}$, is smaller than or equal to a threshold J_th^e ($J_\mathrm{p}^\mathrm{e} \leq J_\mathrm{th}^\mathrm{e}$), the corresponding cell cannot enter the S phase and stay at the G1 or G0 phase until J_p^e becomes larger than J_th^e.

Based on this checkpoint model, we simulated random proliferation with a checkpoint of $J_\mathrm{th}^\mathrm{e} = 0.9$ (Fig. 4 (b)) under the same mechanical condition as in Fig. 4 (a). To highlight the effect of the checkpoint on the mechanical behaviors of the whole tissue, the results of the simulation of random proliferation without a checkpoint (Fig. 4 (c): the same simulation as Fig. 4 (a)) and isotropic hypertrophy (Fig. 4 (d)) were presented. As intended, the proliferation in the constraint lower half of the tissue was suppressed by the influence of the checkpoint, whereas cells actively proliferated in the free upper half, as indicated by the distribution of the cell generation in Fig. 4 (b). Conversely, in cells without the checkpoint, the cell generation was almost uniformly distributed over the tissue (Fig. 4 (c)). Because of this difference in cellular activities, the accumulation of strain energy density was suppressed in cells with checkpoint (Fig. 4 (b)), whereas in cells without checkpoint, the strain energy density accumulated at a single-cell level, especially in the lower half of the tissue (Fig. 4 (c)). In hypertrophic cells, moderate accumulation of strain energy in the lower half was observed (Fig. 4 (d)). Consequently, when the cells proliferated to reach the number of cells $N_\mathrm{p} \sim 2.2 \times 10^5$, which corresponds to 1.5^3 times the number of cells in the initial condition, the whole tissues acquired different shapes depending on the influence of the checkpoint (Fig. 4 (b, c)). This trend was quantitatively examined and illustrated in Fig. 4 (e–g). As the J_th^e became larger, the increasing rate of the number of cells became lower (Fig. 4 (e)), and when compared with the tissues composed of the same number of cells, the total volume and average strain energy density became larger (Fig. 4 (f)) and smaller (Fig. 4 (g)), respectively. Furthermore, these models enabled tracing cells, containing history information, in the growing tissue (Videos 1, 2, and 3). Taken together, these results indicated that the constructed models enabled us to investigate the change in the mechanical behaviors of the whole tissue according to each cellular activity depending on the mechanical state of the cells during morphogenesis.

4. Discussion

In this study, we developed a multiscale method to investigate multicellular tissue morphogenesis by constructing continuum-based particle models that can connect each cellular activity to the mechanical behaviors of the whole tissue. Cell growth and proliferation were explicitly expressed in our models by volume expansion and cell division. These models enabled us to examine the mechanical state of cells that compose the tissue and trace these cells throughout tissue morphogenesis. Incorporating the effect of a checkpoint on a cell cycle into the proliferation model revealed the dependence of the mechanical behaviors of the whole tissue on the condition of cellular activities.

To evaluate the mechanical behaviors of the whole tissue during morphogenesis, various mathematical models of the underlying multicellular dynamics based on continuum mechanics have been proposed and combined with numerical methods such as the FEM (Giorgi et al., 2014; Lipphaus and Witzel, 2019; Vaca-González et al., 2018). However, methods based on FE mesh discretization barely take into account the effect of spatiotemporally heterogeneous cellular activities despite the importance of the heterogeneity of cellular activities for the formation of characteristic tissue shapes. Thus, to take into account the heterogeneous cellular activities at a single-cell level in the continuum-based analysis, we employed the MPM, a continuum-based particle method. A mixed formulation coupling the mass growth and massive deformation based on MPM for simulating growth-induced large deformation behavior of incompressible soft materials has been proposed previously (Zhang et al., 2021). In the present investigation, we extended this method by developing the models of the growth and division of individual cells with an increase in the number of cells in the tissue. The proposed models analyzed the mechanical behaviors of the whole tissue owing to individual cellular activities based on the theory of continuum mechanics.

The MPM based simulation can evaluate the mechanical state of each cell that composed the growing tissue. Therefore, it allows us to consider cellular activities depending on their mechanical state. In this study, we investigated the effect of a checkpoint on a cell cycle that depends on the

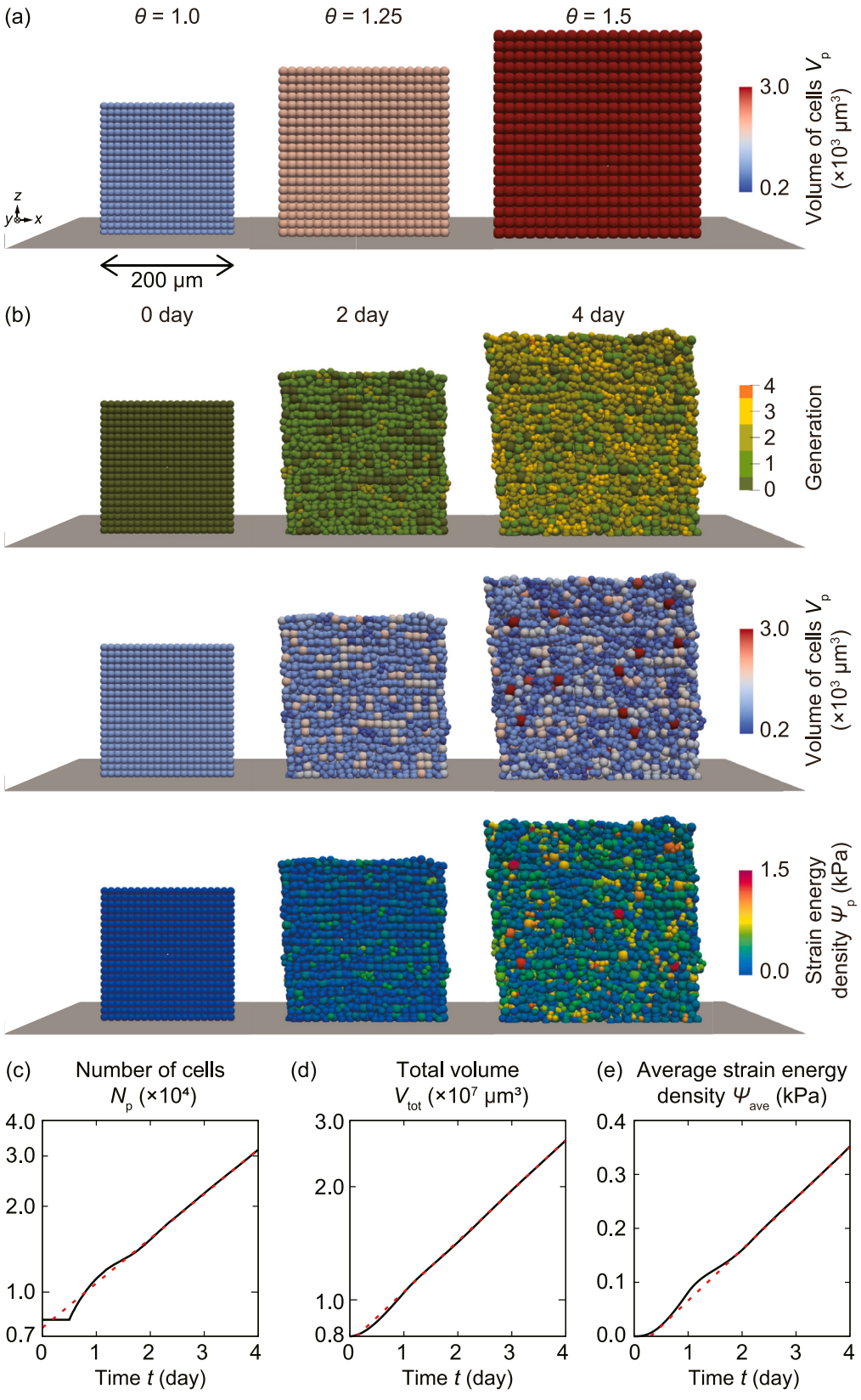

Fig. 3. Cell hypertrophy and proliferation simulation. (a) Change in the cell volume V_p in the growing tissue because of uniform cell hypertrophy. (b) Change in the generation, volume V_p, and strain energy density Ψ_p of cells in growing tissue caused by random proliferation. (c) Change in the number of cells N_p, (d) total volume V_{tot}, and (e) average strain energy density Ψ_{ave} of the growing tissue caused by random proliferation. Dotted orange lines are exponential approximations $N_p = 7500e^{0.36t}$ in (c), $V_{tot} = 7.7 \times 10^6 e^{0.31t}$ (μm³) in (d) and a linear approximation $\Psi_{ave} = 0.095t - 0.029$ (kPa) in (e), fitted for $2.0 \leq t \leq 4.0$.

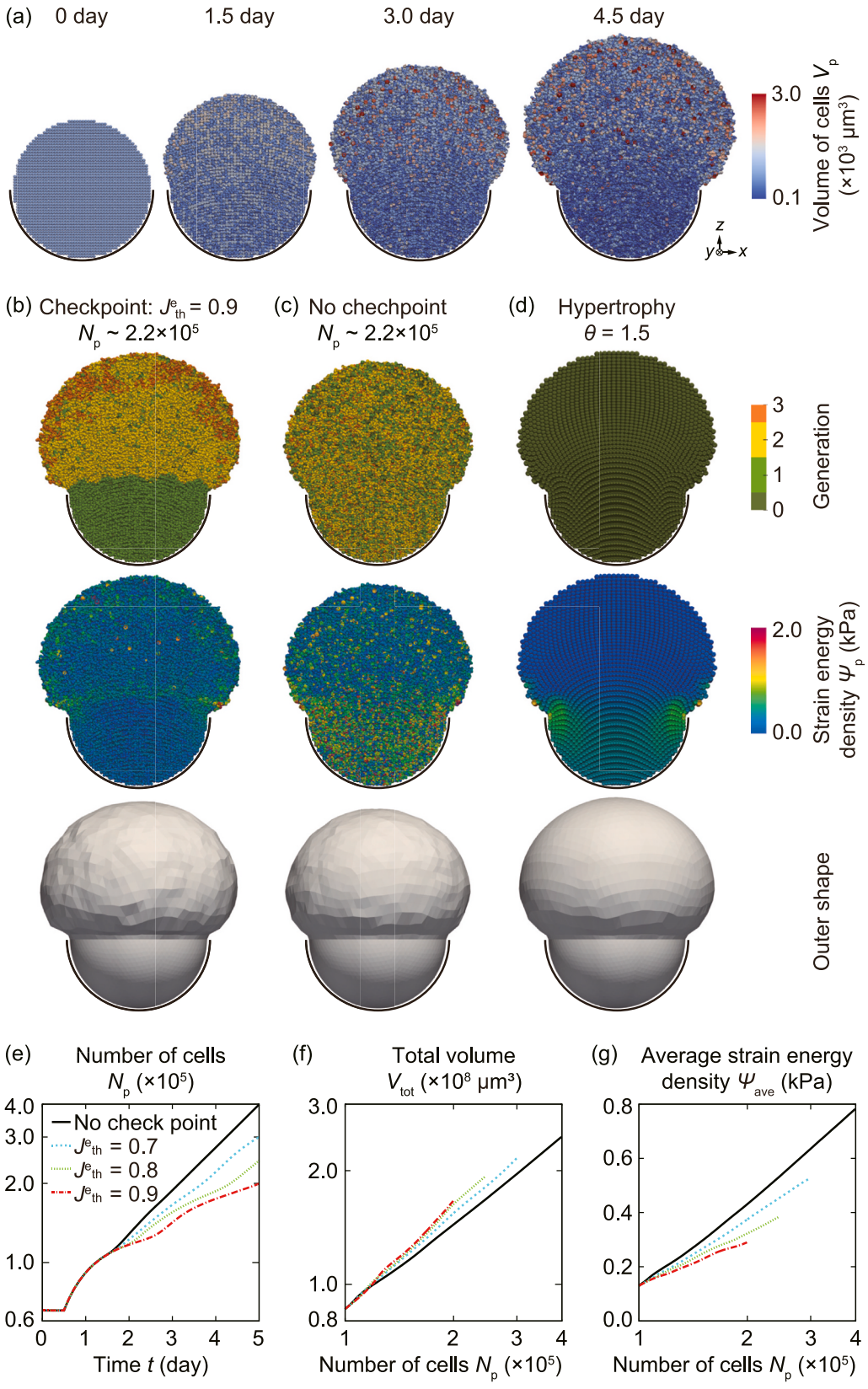

Fig. 4. Simulation of cell proliferation under a constraint condition. (a) Change in cell volume V_p in the growing tissue caused by random proliferation. (b–d) Cell generation, strain energy density Ψ_p, and outer shapes of the tissue under (b) cell proliferation with a checkpoint when $N_p \sim 2.2 \times 10^5$, (c) cell proliferation without a checkpoint when $N_p \sim 2.2 \times 10^5$, and (d) cell hypertrophy at $\theta = 1.5$. (e) Change in the number of cells N_p depending on the checkpoint on a cell cycle. (f) Total volume V_{tot} and (g) average strain energy density Ψ_{ave} of the tissue against the number of cells N_p in the tissue, for 5 days, depending on the checkpoint on a cell cycle.

volume ratio to the initial cell volume (Fig. 4). The cell growth and proliferation models also enabled tracing cells, having information regarding history of division, in the growing tissue (Video 1,2, and 3). Therefore, future extension of the proposed models will allow us to consider cellular activities depending on the history of cell differentiation according to mechanochemical coupling. With these extended models, we would understand the multicellular tissue morphogenesis mechanically.

Supplementary video related to this article can be found at https://doi.org/10.1016/j.jmbbm.2023.105828

One potential application of these models is to simulate the dynamics of multicellular interactions during bone morphogenesis. In developing bone tissue, resting chondrocytes differentiate into proliferative and hypertrophic chondrocytes and form a growth plate (Felsenthal and Zelzer, 2017; Galea et al., 2021; Green et al., 2015; Kronenberg, 2003; Vendra et al., 2018). The resultant bone morphology is determined through the movement of the growth plate with the formation of a calcified bone matrix under mechanical loading. The proposed models will investigate the mechanical behaviors of the growing bone tissue caused by cell hypertrophy and proliferation affected by both mechanical and biochemical environments. Such an investigation will lead to an understanding of the mechanism which determines the bone shapes through multicellular activities. Thus, the proposed models reveal the fundamental biological mechanisms that form physiological and functional tissue shapes, such as bone shapes by regulating cellular activities.

Another possible application of the models is simulating growing organoids (Dahl-Jensen and Grapin-Botton, 2017; Montes-Olivas et al., 2019). The growth simulation of multicellular organoids based on the proposed models will predict changes in their shape under various mechanical conditions of the growth environment. Such an investigation will offer strategies to regulate organoid morphologies by changing the mechanical environment properly during sequential self-organization events. Thus, this study progresses biomedical engineering and regenerative medicine by making organoids with desired shapes and functions.

Not only cell proliferation and hypertrophy but also cell sorting (Townes and Holtfreter, 1955) and extrusion to eliminate apoptotic cells (Katoh and Fujita, 2012) are important for the development and homeostasis of biological tissues, such as embryonic epithelial tissues. The proposed mechanical models can analyze cell displacement according to the whole tissue deformation by considering the biological tissue as a continuum body. Although this assumption of continuum mechanics is reasonable when we consider matrix-rich tissues such as growing bones, incorporating local cell rearrangement into the proposed models will enable us to express various phenomena (e.g., cell sorting). When such an extension of the models is achieved, the proposed simulation models are validated by comparing tissue morphologies and cell movements obtained by the computational analysis based on our models with those observed in *in vitro* experiments. A growing number of studies proposing three-dimensional culture systems of proliferative cancer cells (Yuan et al., 2023) and hypertrophic chondrocytes (Kim et al., 2022) *in vitro* may help validate the proposed models.

The proposed cell growth and proliferation models provide a powerful framework for the investigation of tissue morphogenesis influenced by cellular activities from a mechanical aspect. Thus, further extension of these models may help us understand the regulation mechanism of tissue morphologies in mechanical and biochemical environments and expand the field of developmental biology.

Funding

This work was supported by Grant-in-Aid for Scientific Research (A) (JP20H00659) and (C) (JP22K03827) from Japan Society for the Promotion of Science (JSPS); JST-CREST (JPMJCR22L5); AMED-CREST (Mechanobiology) (JP20gm0810003); and Mori Manufacturing Research and Technology Foundation.

CRediT authorship contribution statement

Yuka Yokoyama: Writing – review & editing, Writing – original draft, Visualization, Validation, Software, Methodology, Investigation, Funding acquisition, Formal analysis, Conceptualization. **Yoshitaka Kameo:** Writing – review & editing, Supervision, Methodology, Funding acquisition, Conceptualization. **Taiji Adachi:** Writing – review & editing, Supervision, Resources, Project administration, Funding acquisition, Conceptualization.

Declaration of competing interest

The authors declare that they have no known competing financial interests or personal relationships that could have appeared to influence the work reported in this paper.

Data availability

Data will be made available on request.

References

Alt, S., Ganguly, P., Salbreux, G., 2017. Vertex models: from cell mechanics to tissue morphogenesis. Phil. Trans. R. Soc. B 372, 20150520. https://doi.org/10.1098/rstb.2015.0520.
Bardenhagen, S.G., Kober, E.M., 2004. The generalized interpolation material point method. CMES - Comput. Model. Eng. Sci. 5, 477–495. https://doi.org/10.3970/cmes.2004.005.477.
Chagnon, G., Rebouah, M., Favier, D., 2015. Hyperelastic energy densities for soft biological tissues: a review. J. Elasticity 120, 129–160. https://doi.org/10.1007/s10659-014-9508-z.
Chanet, S., Miller, C.J., Vaishnav, E.D., Ermentrout, B., Davidson, L.A., Martin, A.C., 2017. Actomyosin meshwork mechanosensing enables tissue shape to orient cell force. Nat. Commun. 8, 15014 https://doi.org/10.1038/ncomms15014.
Charlton, T.J., Coombs, W.M., Augarde, C.E., 2017. iGIMP: an implicit generalised interpolation material point method for large deformations. Comput. Struct. 190, 108–125. https://doi.org/10.1016/j.compstruc.2017.05.004.
Conte, V., Munoz, J., Miodownik, M., 2008. A 3D finite element model of ventral furrow invagination in the Drosophila melanogaster embryo. J. Mech. Behav. Biomed. Mater. 1, 188–198. https://doi.org/10.1016/j.jmbbm.2007.10.002.
Dahl-Jensen, S., Grapin-Botton, A., 2017. The physics of organoids: a biophysical approach to understanding organogenesis. Development 144, 946–951. https://doi.org/10.1242/dev.143693.
Felsenthal, N., Zelzer, E., 2017. Mechanical regulation of musculoskeletal system development. Development 144, 4271–4283. https://doi.org/10.1242/dev.151266.
Galea, G.L., Zein, M.R., Allen, S., Francis-West, P., 2021. Making and shaping endochondral and intramembranous bones. Dev. Dynam. 250, 414–449. https://doi.org/10.1002/dvdy.278.
Giorgi, M., Carriero, A., Shefelbine, S.J., Nowlan, N.C., 2014. Mechanobiological simulations of prenatal joint morphogenesis. J. Biomech. 47, 989–995. https://doi.org/10.1016/j.jbiomech.2014.01.002.
Green, J.D., Tollemar, V., Dougherty, M., Yan, Z., Yin, L., Ye, J., Collier, Z., Mohammed, M.K., Haydon, R.C., Luu, H.H., Kang, R., Lee, M.J., Ho, S.H., He, T.-C., Shi, L.L., Athiviraham, A., 2015. Multifaceted signaling regulators of chondrogenesis: implications in cartilage regeneration and tissue engineering. Genes Dis. 2, 307–327. https://doi.org/10.1016/j.gendis.2015.09.003.
Heer, N.C., Martin, A.C., 2017. Tension, contraction and tissue morphogenesis. Development 144, 4249–4260. https://doi.org/10.1242/dev.151282.
Himpel, G., Kuhl, E., Menzel, A., Steinmann, P., 2005. Computational Modelling of Isotropic Multiplicative Growth. J05-02.
Jamali, Y., Azimi, M., Mofrad, M.R.K., 2010. A sub-cellular viscoelastic model for cell population mechanics. PLoS One 5, e12097. https://doi.org/10.1371/journal.pone.0012097.
Katoh, H., Fujita, Y., 2012. Epithelial homeostasis: elimination by live cell extrusion. Curr. Biol. 22, R453–R455. https://doi.org/10.1016/j.cub.2012.04.036.
Kim, J., Tomida, K., Matsumoto, T., Adachi, T., 2022. Spheroid culture for chondrocytes triggers the initial stage of endochondral ossification. Biotech. Bioeng. ,119, 3311–3318. https://doi.org/10.1002/bit.28203.
Kronenberg, H.M., 2003. Developmental regulation of the growth plate. Nature 423, 332–336. https://doi.org/10.1038/nature01657.
Lipphaus, A., Witzel, U., 2019. Biomechanical study of the development of long bones: finite element structure synthesis of the human second proximal phalanx under growth conditions. Anat. Rec. 302, 1389–1398. https://doi.org/10.1002/ar.24006.
Liu, S., Ginzberg, M.B., Patel, N., Hild, M., Leung, B., Li, Z., Chen, Y.-C., Chang, N., Wang, Y., Tan, C., Diena, S., Trimble, W., Wasserman, L., Jenkins, J.L., Kirschner, M. W., Kafri, R., 2018. Size uniformity of animal cells is actively maintained by a p38 MAPK-dependent regulation of G1-length. Elife 7, e26947. https://doi.org/10.7554/eLife.26947.

Lloyd, A.C., 2013. The regulation of cell size. Cell 154, 1194–1205. https://doi.org/10.1016/j.cell.2013.08.053.

Luo, Q., Kuang, D., Zhang, B., Song, G., 2016. Cell stiffness determined by atomic force microscopy and its correlation with cell motility. Biochim. Biophys. Acta Gen. Subj. 1860, 1953–1960. https://doi.org/10.1016/j.bbagen.2016.06.010.

Matejčić, M., Trepat, X., 2022. Mechanobiological approaches to synthetic morphogenesis: learning by building. Trends Cell Biol. 33 (2), 95–111. https://doi.org/10.1016/j.tcb.2022.06.013.

Montes-Olivas, S., Marucci, L., Homer, M., 2019. Mathematical models of organoid cultures. Front. Genet. 10, 873. https://doi.org/10.3389/fgene.2019.00873.

Osborne, J.M., Fletcher, A.G., Pitt-Francis, J.M., Maini, P.K., Gavaghan, D.J., 2017. Comparing individual-based approaches to modelling the self-organization of multicellular tissues. PLoS Comput. Biol. 13, e1005387 https://doi.org/10.1371/journal.pcbi.1005387.

Pan, S., Yamaguchi, Y., Suppasri, A., Moriguchi, S., Terada, K., 2021. MPM–FEM hybrid method for granular mass–water interaction problems. Comput. Mech. 68, 155–173. https://doi.org/10.1007/s00466-021-02024-2.

Shwartz, Y., Farkas, Z., Stern, T., Aszódi, A., Zelzer, E., 2012. Muscle contraction controls skeletal morphogenesis through regulation of chondrocyte convergent extension. Dev. Biol. 370, 154–163. https://doi.org/10.1016/j.ydbio.2012.07.026.

Stomakhin, A., Schroeder, C., Chai, L., Teran, J., Selle, A., 2013. A material point method for snow simulation. ACM Trans. Graph. 32, 1–10. https://doi.org/10.1145/2461912.2461948.

Takeda, H., Kameo, Y., Inoue, Y., Adachi, T., 2019. An energy landscape approach to understanding variety and robustness in tissue morphogenesis. Biomech. Model. Mechanobiol. 19, 471–479. https://doi.org/10.1007/s10237-019-01222-5.

Townes, P.L., Holtfreter, J., 1955. Directed movements and selective adhesion of embryonic amphibian cells. J. Exp. Zool. 128, 53–120. https://doi.org/10.1002/jez.1401280105.

Trickey, W.R., Baaijens, F.P.T., Laursen, T.A., Alexopoulos, L.G., Guilak, F., 2006. Determination of the Poisson's ratio of the cell: recovery properties of chondrocytes after release from complete micropipette aspiration. J. Biomech. 39, 78–87. https://doi.org/10.1016/j.jbiomech.2004.11.006.

Trubuil, E., D'Angelo, A., Solon, J., 2021. Tissue mechanics in morphogenesis: active control of tissue material properties to shape living organisms. Cells Dev. 168, 203777 https://doi.org/10.1016/j.cdev.2022.203777.

Vaca-González, J.J., Moncayo-Donoso, M., Guevara, J.M., Hata, Y., Shefelbine, S.J., Garzón-Alvarado, D.A., 2018. Mechanobiological modeling of endochondral ossification: an experimental and computational analysis. Biomech. Model. Mechanobiol. 17, 853–875. https://doi.org/10.1007/s10237-017-0997-0.

Vendra, B.B., Roan, E., Williams, J.L., 2018. Chondron curvature mapping in growth plate cartilage under compressive loading. J. Mech. Behav. Biomed. Mater. 84, 168–177. https://doi.org/10.1016/j.jmbbm.2018.05.015.

Voss-Böhme, A., 2012. Multi-scale modeling in morphogenesis: a critical analysis of the cellular Potts model. PLoS One 7, e42852. https://doi.org/10.1371/journal.pone.0042852.

Xie, S., Skotheim, J.M., 2020. A G1 sizer coordinates growth and division in the mouse epidermis. Curr. Biol. 30, 916–924.e2. https://doi.org/10.1016/j.cub.2019.12.062.

Yamaguchi, Y., Moriguchi, S., Terada, K., 2021. Extended B-spline-based implicit material point method. Int. J. Numer. Methods Eng. 122, 1746–1769. https://doi.org/10.1002/nme.6598.

Yuan, J., Li, X., Yu, S., 2023. Cancer organoid co-culture model system: novel approach to guide precision medicine. Front. Immunol. 13, 1061388. https://doi.org/10.3389/fimmu.2022.1061388.

Zhang, Z., Pan, Y., Wang, J., Zhang, H., Chen, Z., Zheng, Y., Ye, H., 2021. A total-Lagrangian material point method for coupled growth and massive deformation of incompressible soft materials. Num. Meth Eng. 122, 6180–6202. https://doi.org/10.1002/nme.6787.